Determination of interface fracture properties by micro-and macro-scale experiments in nacre-like alumina

Aurélien Doitrand, Ronan Henry, Hassan Saad, Sylvain Deville, Sylvain Meille

Determination of interface fracture properties by micro- and macro-scale experiments in nacre-like alumina

Aurelien Doitrand[a,*], Ronan Henry[a], Hassan Saad[b], Sylvain Deville[b,c], Sylvain Meille[a]

[a] *Université Lyon, INSA-Lyon, MATEIS UMR CNRS 5510, F-69621 Villeurbanne Cedex, France*
[b] *Laboratoire de Synthèse et Fonctionnalisation des Céramiques, UMR 3080 CNRS/Saint-Gobain, Saint-Gobain Research Provence, Cavaillon, France*
[c] *now with: Université de Lyon, Université Claude Bernard Lyon 1, CNRS, Institut Lumière Matière, 69622 Villeurbanne, France*

Abstract

The mechanical properties of brick-and-mortar composites depend on their interface fracture properties, which have not been evaluated to date, preventing a rational optimization of the microstructure and of the resulting mechanical properties. Micro-(cantilever) and macro-scale (Single Edge Notched Bending) tests on nacre-like alumina both result in crack initiation at the interface between the platelets. We assess crack initiation and predict the failure force by means of 2D and 3D finite element simulations employing the same fracture modeling approach at both scales, namely the coupled criterion. The interface fracture properties are determined by means of inverse identification based on both micro- and macro-scale experiments. The interface exhibits typical values of 625 MPa tensile strength and 1.9 J/m^2 toughness. The forces at crack initiation predicted employing these parameters are in good agreement with the forces measured experimentally for both micro- and macro-scale tests. The quantitative determination of the interface fracture properties should help the design and optimization of this class of brick-and-mortar materials.

Keywords: Nacre-like alumina; Interface failure; Crack initiation; Coupled criterion

1. Introduction

Monolithic ceramics exhibit high strength and stiffness but also a brittle failure behavior at ambient temperature, often limiting their range of application. One way to overcome this

*Corresponding author
Email address: aurelien.doitrand@insa-lyon.fr (Aurelien Doitrand)

issue is the design of materials inspired from natural structures. For instance, natural nacre is an example of material which almost exclusively consists of brittle constituents but has a non brittle macroscopic behavior [1, 2, 3] due to its brick-and-mortar microstructure with a macroscopic toughness 40 times larger than its main constituent, aragonite [4]. This increase in toughness results from microstructural features such as, for instance, bridges between bricks, brick thickness variation and self-locking shape, which promote crack deflection, branching or microcracking [5]. Inspired from the brick-and-mortar microstructure, nacre-like inorganic composites consist of a dense and ordered packing of micron-sized ceramic platelets and of a secondary phase at the interface between the platelets. Details about nacre-like alumina processing, structure and macroscopic mechanical properties can be found in a recent review [6]. The apparent macroscopic behavior of nacre-like composites strongly depends on the secondary phase constituents [7] and on fracture mechanisms of the material microstructure. For instance, crack deflection and branching at interfaces may lead to a non-brittle macroscopic behavior [7, 8, 9]. These mechanisms ensure larger created crack surfaces and thus larger energy dissipation than for a straigth crack propagation through the platelets.

Nacre-like composite microstructure may be optimized in order to promote such fracture mechanisms and thus enhance the apparent macroscopic toughness increase. Numerical simulations at the building block scale may help understand the influence of key microstructural features and provide guidelines for the microstructure optimization, for instance by means of periodic cell modeling [10, 11, 12, 13, 14]. Begley *et al.* [10] developed a micromechanical model taking into account elastic perfectly plastic interfaces. They showed that vertical interfaces contribute to the overall composite stiffness and influences the peak strength in case of short bricks. They also highlighted that optimal peak strength, stiffness and work to failure could be optimized by adjusting simultaneously the brick size and the interface yield strength. Employing molecular mechanics framework, Dimas and Buehler [11] showed the need to ensure a 0.3 to 0.6 interface to brick stiffness ratio in order to both maintain a stiff system and avoid brittle fracture. Barthelat [12] set up a step-by-step optimization for the design of staggered composites that resulted in guidelines concerning the size, properties and volume content of the tablets, the interface strength and platelet overlap. A resulting design recommandation was, for instance, a high platelet volume fraction with platelets five time

stronger than the interface. Discrete element modeling was recently used [13, 14] to simulate fracture in brick-and-mortar structures. Abid *et al.* [13] highlighted the importance to control the architecture in order to minimize statistical microstructure variations and concluded that interfaces with large fracture toughness to strength ratio are more likely to maximize energy dissipation. Radi *et al.* [14] investigated the influence of the interface strength on the macroscopic toughness and maximum stress and derived guidelines for their optimization.

It is clear that simulation can help to draw qualitative conclusions and guidelines by investigating the influence of some parameters of the numerical models. However, quantitative predictions require the knowledge of the stiffness, strength and toughness of the constituents required by numerical models for their fracture modeling.

Single edge notched bending is classically used to characterize the macroscopic behavior of nacre-like alumina, and especially their equivalent fracture toughness [6, 7, 15, 16] but it has not been used so far to try to determine the constituent properties. Specific tests at the constituent scale have been developed in order to characterize the nacre-like constituent properties. Feilden *et al.* [17] tested single micron-scale alumina platelets under three-point bending and determined that they could locally sustain stresses up to 5GPa. Based on these experiments, we *et al.* [18] showed that such high stress levels can be locally reached because of the small platelet size, for which failure is mainly driven by an energy criterion and thus the platelet fracture toughness. We determined that the platelets exhibit G_c =20 J/m^2 fracture energy and σ_c = 1.1 GPa strength (defined as a material properties that does not depend on any geometrical features [18]) by means of inverse identification procedure and failure modeling employing a coupled stress and energy criterion [19, 20]. Recently, Henry *et al.* [21] set-up micron-scale experiments to characterize the fracture properties of the interface between the platelets. Such tests are performed at a very small scale and require appropriate post-processing in order to deduce the constituent properties from the measured data. The same fracture modeling approach as the one used for platelet failure prediction [18], namely the coupled criterion (CC), allows to assess interface fracture. For instance, interface debonding was studied in composite materials [22, 23, 24, 25, 26, 27] as well as failure at bonded joints [28, 29, 30, 31, 32] by means of the CC. A numerical implementation of the CC for elastic interfaces has also recently been proposed by Muñoz *et al.* [33].

The objective of this work is to determine the interface properties of the nacre-like composite using both micro- and macro-scale tests and numerical modeling of fracture at both scales. Experiments taken from [16, 21] are presented in Section 2. Section 3 is dedicated to the CC for fracture modeling. The finite element models are described in section 4. Finally, the nacre-like interface strength and fracture energy are determined in Section 5 and numerical results are compared to experimental data.

2. Experiments

2.1. Material and specimen preparation

The material under investigation, a nacre-like ceramic composite, is obtained from a system consisting of anisotropic alumina platelets, alumina nanoparticles and glass phase [7]. The platelet shape is hexagonal, with about 0.5 μm thickness and 5 to 10 μm diameter (Figs. 1 and 2). The platelets are not perfectly monocrystalline since they may contain $\approx$50 nm thick defective region [17]. They exhibit a trigonal crystal system and the corresponding stiffness matrix is given in Eqn. (1) with C_{11}=466 GPa, C_{12}=127 GPa, C_{13}=117 GPa, C_{14}=94 GPa, C_{33}=506 GPa, C_{44}=235 GPa and C_{66}=170 GPa [34]. In the sequel, the axis system (O,$\vec{e_1}$,$\vec{e_2}$,$\vec{e_3}$) always refers to the platelet local axis system so that direction 3 coincides with the platelet c-axis (Figs. 1 and 2).

The manufacturing process leading to the brick-and-mortar microstructure of the material is described in details in [16]. The platelets are aligned in a preferential direction perpendicular to the platelet c-axis by imposing uniaxial pressure during sintering. It results in a

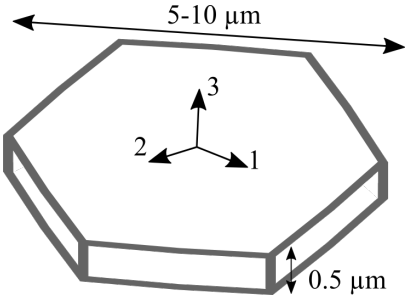

Figure 1: Dimensions of the platelet. Direction 3 corresponds to the platelet c-axis.

$$\underline{\underline{C}} = \begin{pmatrix} C_{11} & C_{12} & C_{13} & C_{14} & 0 & 0 \\ C_{12} & C_{11} & C_{13} & -C_{14} & 0 & 0 \\ C_{13} & C_{13} & C_{33} & 0 & 0 & 0 \\ C_{14} & -C_{14} & 0 & C_{44} & 0 & 0 \\ 0 & 0 & 0 & 0 & C_{44} & C_{14} \\ 0 & 0 & 0 & 0 & C_{14} & \frac{C_{11}-C_{12}}{2} \end{pmatrix} \quad (1)$$

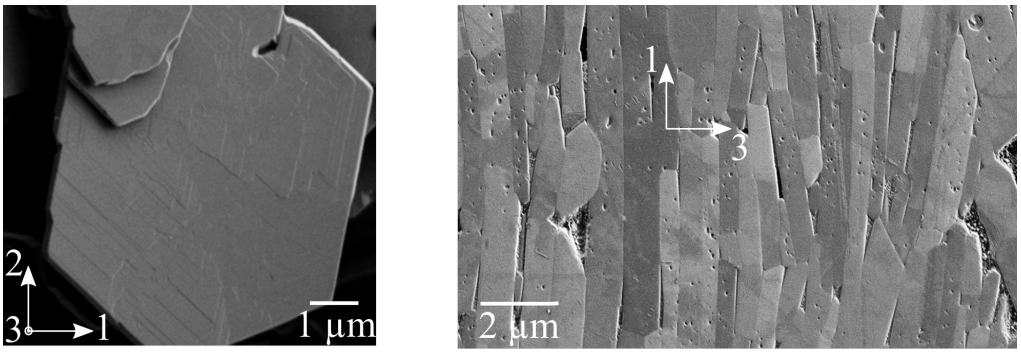

Figure 2: SEM observations and axis system of (Left) a single platelet and (Right) a pack of aligned platelets in the sintered microstructure.

long range alignment of the platelets even if some defects due to local platelet misalignment can be encountered. The average misalignment measured using EBSD is 15 deg (Fig. 2) with respect to the mean alignment direction. The thickness of the interfaces between the platelets is around 2 to 10 nm depending on the distribution of the glass-phase and the presence of nano-bridges. The material exhibits a macroscopic transversely isotropic behavior. Ultrasonic contact technique provides E_T=320 GPa Young's modulus and ν_{TT}=0.24 Poisson's ratio in the platelet plane ((O,$\vec{e_1}$,$\vec{e_2}$) in Fig. 2), and E_L=368 GPa Young's modulus and ν_{LT}=0.24 Poisson's ratio in the platelet thickness direction(direction 3 in Fig. 2) [16]. In Sections 2.2 and 2.3, we describe the experiments [16, 21] on which the interface fracture property identification is based.

2.2. Micron scale cantilever

Micro-cantilever specimens with a pentagonal section are prepared using a Focalized Ion Beam (FIB) [21]. Fig. 3 displays a SEM observation of a specimen and the dimensions of the specimen. The specimen milling was controlled so that the platelet c-axis is rotated by a given angle θ with respect to the beam neutral axis (Fig. 3b). Several specimens with θ between 0 deg. and 56 deg. are tested under bending using a nano-indenter with optical microscope aiming system. All the tested specimens exhibit a linear variation of the force as a function of the displacement up to failure. The tested specimen dimensions and the corresponding failure force are given in Tab. 1, the force measurement uncertainty being γ_{micro}=10 μN. For all the specimens, failure occurs at the interface between platelets. The

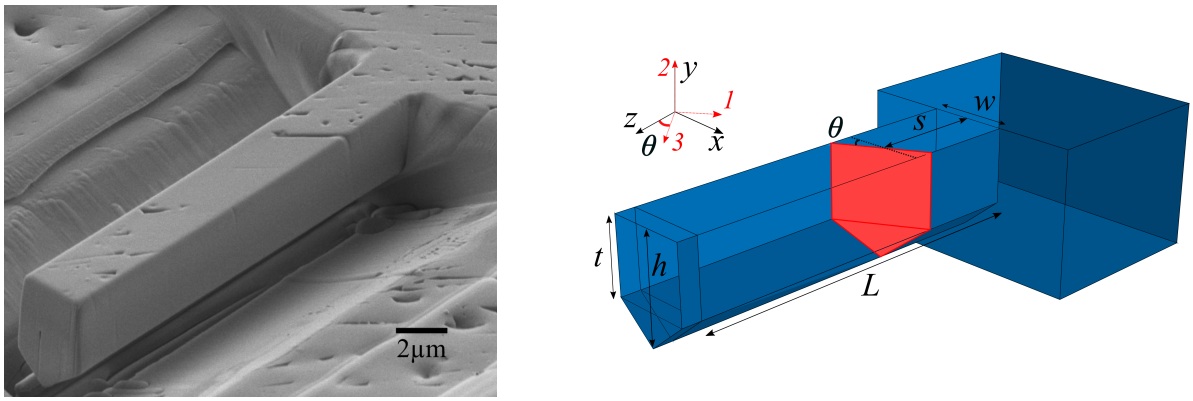

Figure 3: (Left) SEM observation of the specimen with θ=45 deg. angle between platelet c-axis and the beam neutral axis. (Right) Dimensions of the specimen, the beam neutral axis is along (Oz) direction and θ is the angle between the beam neutral axis and the platet c-axis. The interface fracture plane is colored in red.

θ (deg.)	w (μm)	t (μm)	h (μm)	s (μm)	L (μm)	Fc (mN)
0	3.65	2.46	4.26	1.87	20.19	0.26
10	2.02	2.75	3.68	1.65	17.27	0.19
12	4.18	4.08	5.52	5.27	18.91	1.07
26	4.12	3.44	5.01	1.34	17.13	0.98
45	3.22	3.86	5.29	3.21	20.77	1.06
56	3.46	4.53	6.51	2.24	27.36	1.52

Table 1: Dimensions and failure force measured experimentally for micro-cantilever specimens.

fracture surface of the specimen with $\theta = 45$ deg. platelet c-axis angle with respect to the beam neutral axis is shown in Fig. 4. It can be observed that the fracture surface follows the interfaces between platelets, it is thus not perfectly plane and may present some small steps depending on the local platelet arrangement.

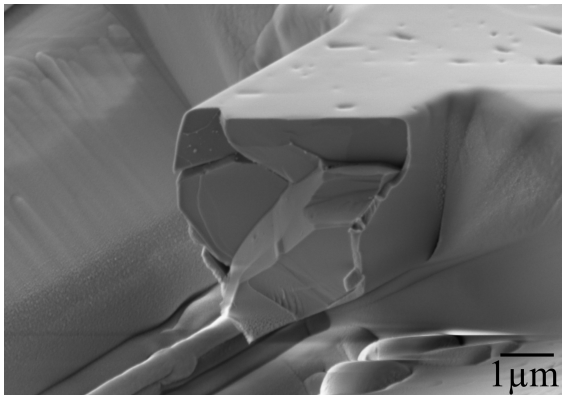

Figure 4: SEM observation of the fracture surface of the specimen with θ=45 deg. angle between platelet c-axis and the beam neutral axis.

2.3. Single-Edge notched beam tests

Four point Single Edge Notched Beam (SENB) tests are performed in order to study crack initiation at the macroscopic scale [16]. Fig. 5 displays a photograph and a sketch of the specimen with its dimensions. Five sets of specimens containing a blunted notch are tested, the specimen dimensions are given in Tab. 2 together with the corresponding range of measured force at crack initiation. The force measurement uncertainty is γ_{SENB}=2 N. Macroscopic observations of the specimen after failure show that the cracks are oriented at between 70 deg. and 80 deg. with respect to the plane at mid specimen length (Fig. 6a). However, a detailed observation around the initial notch shows that crack initiation seems to occur at the interface between the platelets, almost perpendicularly to the plane at mid specimen length (Fig. 6b-c).

In homogeneous isotropic materials, the crack would initiate and propagate along the initial notch direction since it corresponds to the direction ((O,$\vec{e_1}$) in Fig. 6) of the maximum opening stress (σ_{11}) . However, there are also secondary opening (σ_{33} in Fig. 6) and shear (σ_{13} in Fig. 6) stress maxima that are not located at the notch tip but rather between the notch tip and the straight edge to notch tip transition [21]. The ratio between these secondary stress maxima magnitude and the maximum opening stress maximum magnitude is around 0.4 [21]. Therefore, in anisotropic materials such as nacre-like composites, crack

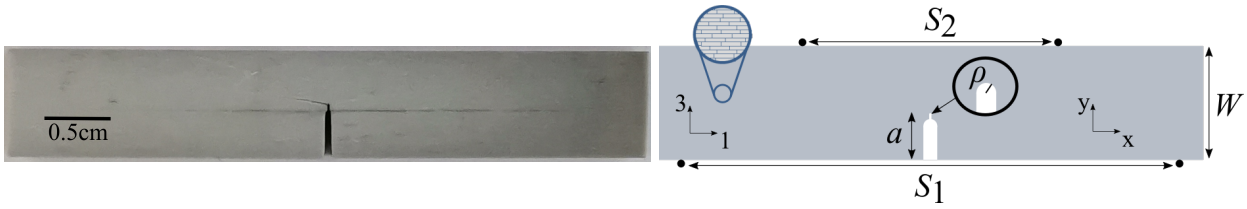

Figure 5: (Left) Photograph of a SENB specimen. (Right) Geometry and dimension of the specimen highlighting the orientation of the platelets in the specimen.

Type	W (mm)	B (mm)	S_1 (mm)	S_2 (mm)	a (mm)	ρ (μm)	Fc (N)
1 (4 Specimens)	5.00±0.01	2.00±0.01	24.00±0.01	6.00±0.01	2.41±0.17	30.00±6.00	86.14±12.02
2 (4 Specimens)	6.00±0.01	3.00±0.01	28.00±0.01	7.00±0.01	2.73±0.12	28.50±2.50	165.98±9.92
3 (5 Specimens)	7.01±0.01	3.50±0.01	32.00±0.01	8.00±0.01	3.23±0.09	36.00±7.00	204.32±17.10
4 (6 Specimens)	8.00±0.01	4.01±0.01	40.00±0.01	10.00±0.01	3.90±0.14	39.50±8.50	217.38±22.19
5 (2 Specimens)	10.08±0.01	4.98±0.01	48.00±0.01	12.00±0.01	5.02±0.05	39.50±8.50	330.64±5.77

Table 2: Dimensions and failure force measured experimentally for SENB specimens, B is the specimen thickness.

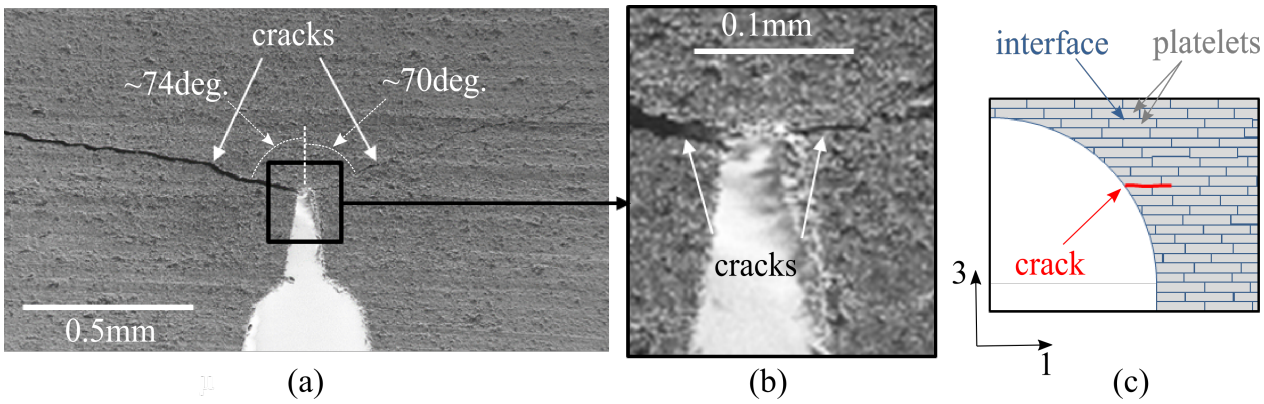

Figure 6: (a) Microscope observation of the specimen after failure and (b) focus around the notch. (c) Diagram of notch crack initiation at the interface between platelets.

initiation location and direction at the notch depends on the material fracture parameters along different directions. Given the position of the platelets with respect to the notch, crack initiation along (O,$\vec{e_1}$) direction corresponds to interface fracture, whereas crack initiation along (O,$\vec{e_3}$) direction would rather involve platelet failure. We showed in a previous work [18] that due to their small dimensions, platelet failure require substantially high loading corresponding to local stress levels as large as 5 GPa. Crack initiation along the interface may thus be explained by the secondary opening and shear stress maxima and the material exhibiting anisotropic failure properties due to the platelet arrangement.

After initiation, crack propagation and deviation along the interfaces between platelets results in a macroscopic crack slanted with respect to the specimen middle plane.

3. Fracture modeling

3.1. The coupled criterion

Crack nucleation assessment under quasi-static loading using the coupled criterion relies on the simultaneous fulfilment of both stress and energy conditions [19]. On the one hand, just before crack nucleation, the stress must be sufficiently high over the whole area corresponding to the initiation crack. On the other hand, the potential energy released ($-\Delta W$) by the crack opening must be larger than the energy required for crack nucleation: $G_c \times S$, where G_c is

the material fracture toughness and S the crack surface. The two conditions write:

$$\begin{cases} f(\underline{\sigma}, \sigma_c, \tau_c) \geqslant 1, \\ G_{inc} = \frac{-\Delta W}{S} \geqslant G_c. \end{cases} \tag{2}$$

where G_{inc} is the incremental energy release rate. In isotropic materials, the crack selects the direction where it is subjected to maximum opening. However, crack initiation along an interface involves both opening and shear, therefore the stress criterion f is a function of the stress tensor $\underline{\sigma}$ and the shear (τ_c) and tensile (σ_c) strengths. Defining the shear to tensile strength ratio $\alpha = \frac{\tau_c}{\sigma_c}$, we choose a stress criterion so that:

$$f(\underline{\sigma}, \alpha, \sigma_c) = \max(\frac{\sigma_{nn}}{\sigma_c}, \frac{|\sigma_{nt}|}{\tau_c}) = \frac{1}{\sigma_c}\max(\sigma_{nn}, \frac{|\sigma_{nt}|}{\alpha}) \geqslant 1 \tag{3}$$

where σ_{nn} and σ_{nt} are respectively the interface opening and shear stresses. The stress criterion thus rewrites:

$$\sigma_{eq} = \max(\sigma_{nn}, \frac{|\sigma_{nt}|}{\alpha}) \geqslant \sigma_c, \tag{4}$$

which must be fulfilled over the whole crack area to make crack initiation possible. The choice of such a criterion rather than a quadratic criterion is supported by considerations about the stress state at failure [21]. It was also already successfully employed in a previous study to predict crack initiation at scarf joints using the CC [31].

Under the assumption of linear elasticity and small deformations, exploiting the stress and potential energy proportionality to the applied displacement (denoted U_0) and the square applied displacement respectively, these conditions write:

$$\sigma_{eq}(S) = \xi(S)U_0 \geqslant \sigma_c, \tag{5}$$

and:

$$G_{inc}(S) = -\frac{\Delta W}{S} = A(S)U_0^2 \geqslant G_c, \tag{6}$$

where ξ and A are two functions depending on specimen geometry and material behavior. The imposed displacement at crack initiation U_c corresponds to the smallest imposed displacement

U_0 for which both the stress and the energy conditions are fulfilled.

Both studied crack initiation cases (micro-cantilever and SENB) correspond to the classical situation of monotonically increasing incremental energy release rate and monotonically decreasing stress as a function of the crack surface. Therefore, we determine the crack surface at initiation S_c by combining and solving Eqn. (5) and Eqn. (6), which yields:

$$\frac{A(S_c)}{\xi(S_c)^2} = \frac{G_c}{\sigma_c^2}. \tag{7}$$

Then, the initiation imposed displacement can then obtained using either Eqn. (5) or (6)

$$U_c = \sqrt{\frac{G_c}{A(S_c)}} = \frac{\sigma_c}{\xi(S_c)}. \tag{8}$$

Note that all the equations have been written for the 3D case as a function of the crack surface S. The CC solution in a 2D case uses the same equations with the difference that the crack surface S is replaced by the crack length l. In the sequel, both 2D and 3D applications of the CC are presented.

3.2. 2D implementation

Two dimensional crack initiation can usually be assessed involving two parameters describing the crack, namely its direction and its length. For the studied SENB case, crack initiation direction is known since it follows the platelet interface (direction (O,$\vec{e_1}$) in Fig. 6), therefore we only need one parameter to describe the crack: its length.

Crack initiation length can be determined solving Eqn. (7) which requires the calculation of the functions A and ξ. Only one calculation without crack is necessary to compute the stress without crack and thus ξ, whereas the calculation of A requires the calculation of the potential energy variation for several crack lengths. This is done by successively unbuttoning the nodes lying on the crack path. Once the functions ξ and A are determined, solving Eqn. (7) only requires to implement the material fracture toughness G_c and strength σ_c. Therefore, it is convenient to vary G_c and strength σ_c since it does not require any supplementary FE calculations. It only requires solving Eqn (7) again for the new (G_c, σ_c) couple, which makes the CC really efficient for inverse identification approaches.

Finally, the steps to solve the CC can be summarized as follows:

1) Calculate the stress without crack along the crack path and compute ξ.

2) Calculate the potential energy variation for several crack lengths and compute A.

3) Solve Eqn. (7) for given G_c and σ_c to determine the initiation crack length.

4) Determine the initiation imposed displacement using Eqn. (8).

3.3. 3D implementation

The main difference between 2D and 3D implementations of the CC concerns the crack surface definition. Whereas in 2D, it is straightforward to define the crack length, a 3D crack may theoretically be described by an infinite number of parameters. To overcome this issue, Doitrand and Leguillon [31, 32, 35, 36] suggested to define the possible initiation crack shapes based on the stress field isocontours. This method presents the major advantage to describe the 3D crack shape by a single parameter, for instance the crack surface or the crack length in a given direction. Otherwise, the approach may become computationally more costly, especially if the crack is described by several parameters [24]. Moreover, it is consistent with the stress criterion employed in the CC: this definition of the possible initiation cracks ensures that the stress criterion is strictly fulfilled over the whole initiation crack surface. Once the possible crack shapes are determined based on the stress field isocontours, they must be inserted in the initial specimen geometry to create a mesh that includes lines corresponding to these isocontours. Then, the nodes are doubled over the area corresponding to each crack shape in order to compute the potential energy variation.

Finally, the steps to solve the CC in 3D can be summarized as follows:

1) Calculate the stress without crack in the crack plane and compute ξ.

2) Define the possible initiation crack shapes based on the stress isocontours.

3) Include the possible initiation crack shapes in the geometry and obtained a mesh including these crack lines.

4) Calculate the potential energy variation for several crack surfaces and compute A.

5) Solve Eqn. (7) for given G_c and σ_c to determine the initiation crack length.

6) Determine the initiation imposed displacement using Eqn. (8).

4. Fracture simulation at micro- and macro-scale

This section describes FE modeling of both micro- (3D modeling) and macro-scale (2D modeling) specimens in order to calculate the ingredients required to solve the CC.

4.1. Finite element model of micro-cantilever

A FE model of micro-cantilever is set up using Abaqus^{TM}. The dimensions of the specimen are depicted in Fig. 3. The normal to the crack plane makes an angle theta with the beam neutral axis (Oz) in (Oxz) plane. Dirichlet boundary conditions are imposed in order to simulate the indenter induced beam bending. A local displacement in (Oy) direction is imposed at the location of the contact between the indenter and the specimen. The area where the beam is clamped is also modeled, with a null imposed normal displacement on its external faces.

Since the thickness of the interface between platelets is around 100 times smaller than the platelet thickness, we do not explicitly model the interfaces in the FE model and consider them as infinitesimally small. Therefore, we simulate fracture occurring at these zero-thickness interfaces by taking into account the interface fracture properties in the CC. We also make the assumption that due to the interface smallness with respect to the platelet thickness, the stiffness of the beam is that of the platelet. We thus adopt the platelet elastic behavior described in Section 2 for the beam. The local orientation of the platelet is defined so that the normal to platelet interface (corresponding to the platelet c-axis direction) is obtained by a rotation of angle θ around (Oy). The mesh consists of 10-nodes tetrahedrons and it is refined near the interface fracture plane (Fig. 7). A first calculation without crack is

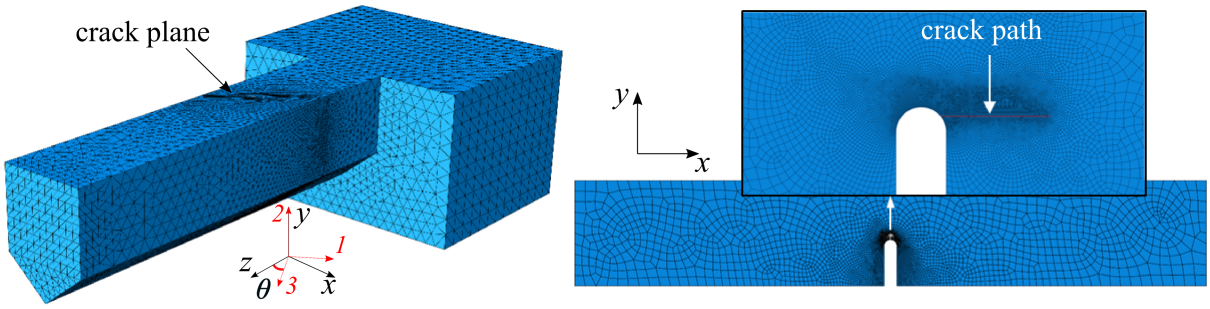

Figure 7: FE mesh of (Left) micron-scale cantilever and (Right) SENB specimens.

performed in order to determine the stress fields on the crack plane, which allows computing ξ as a function of the corresponding crack surface S. An example of possible initiation crack shapes based on the stress field isocontours is depicted in Fig. 8 for $\theta = 45$ deg. and $\alpha = 1$. Fig 8a shows the stress field σ_{eq} and the corresponding isocontours are depicted in Fig 8b. The lines corresponding to the isocontours are added to the geometry (Fig. 8c) so that the mesh includes the possible crack shapes used for the potential energy variation calculation as a function of the crack surface. The nodes lying on the surfaces delimited by the isocontour lines are successively unbuttoned to compute the potential energy for several crack surfaces, which allows computing A as a function of the crack surface.

Fig. 9a shows a graphical representation of Eqn. (7) for α=1, θ =0 deg., G_c =5 J/m^2 and σ_c=900 MPa. The crack initiation surface is determined as the intersection of the two curves representing each side of the equation. Another way to determine the initiation surface and imposed displacement consists in determining the minimum imposed displacement U_0 so that there exists a crack surface for which both the stress and the energy criteria are fulfilled. This can be graphically represented by studying the variation of the incremental energy release rate to fracture toughness and stress to strength ratios (Fig. 9b-c). If the imposed displacement is too small, the intersection between the crack surface set for which the stress criterion is fulfilled and the one for which the energy criterion is fulfilled is empty (Fig. 9b), therefore crack initiation cannot occur. The minimum imposed displacement for which the intersection between both sets is not empty (it contains a single crack surface that is the initiation crack

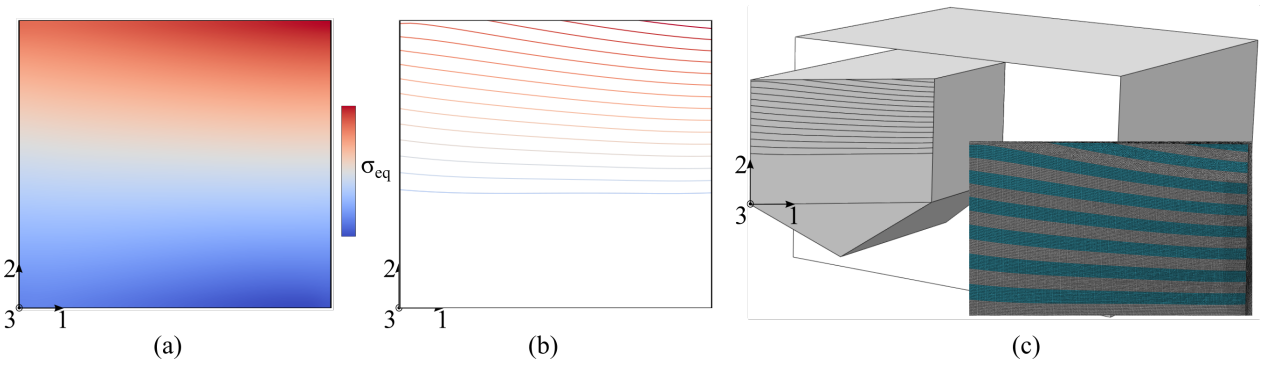

Figure 8: Stress (a) field and (b) isocontours (the bottom isocontour corresponds to $\sigma_{eq} = 0$) (c) geometry and mesh including the isocontour-based crack shapes (one out of two is colored in blue for visualization purpose).

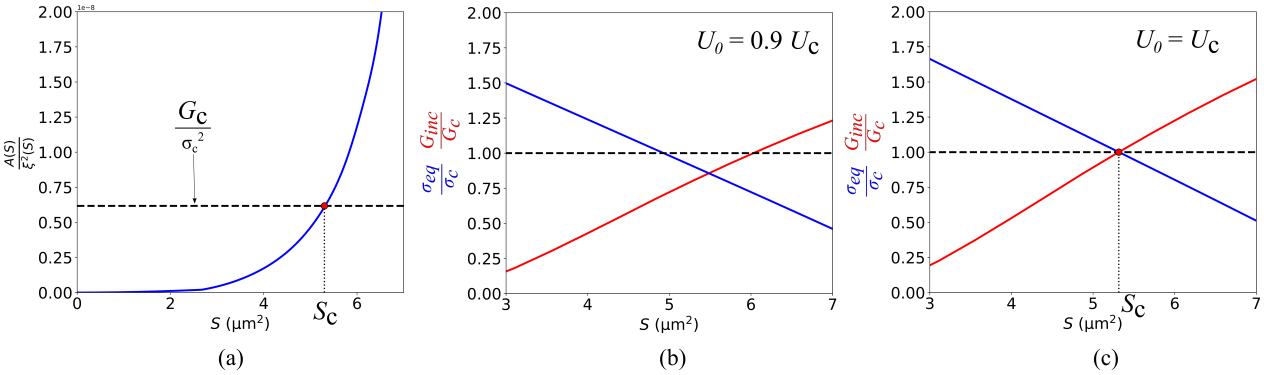

Figure 9: (a) Graphical solution of Eqn. (7) allowing the determination of the initiation crack surface S_c. (b-c) Incremental energy release rate to fracture toughness and stress to strength ratios as a function of the crack surface for an imposed displacement (b) smaller than the initiation displacement (both criteria are not simultaneously met for any crack surfaces) and (c) equal to the initiation displacement (both criteria are fulfilled for $S = S_c$).

surface) is the initiation imposed displacement (Fig. 9c).

4.2. Finite element model of SENB

A FE model of SENB is set up according to the specimen dimensions depicted in Fig. 5. The crack path lies along (Ox) direction so as to reproduce crack initiation at an interface between platelets which c-axis is oriented along (Oy) direction. The crack path is located at a distance $\rho/2$ of the notch tip in (Oy) direction. Dirichlet boundary conditions are imposed in order to simulate the four point bending. A displacement in (Oy) direction is imposed at the location of the contact between the spans and the specimen and it is set to zero at the location of the contact between the supports and the specimen. A transversely isotropic behavior is adopted with the properties given in Section 2.1. The shear modulus is set to G_{LT} =148 GPa. The local orientation is defined so that the normal to the platelet lies in (Oy) direction. Similarly to micro-scale specimen simulation, we consider the interface as infinitesimally small.

The mesh consisting of 4-nodes elements is refined near the crack path (Fig. 7). Calculations with several crack lengths are successively performed in order to compute the potential energy variation as a function of the crack length. The stress variation along the crack path is computed in the case without crack. Fig. 10 depicts both the graphical solution to Eqn. (7) and the stress to strength and incremental energy release rate to fracture toughness ratios

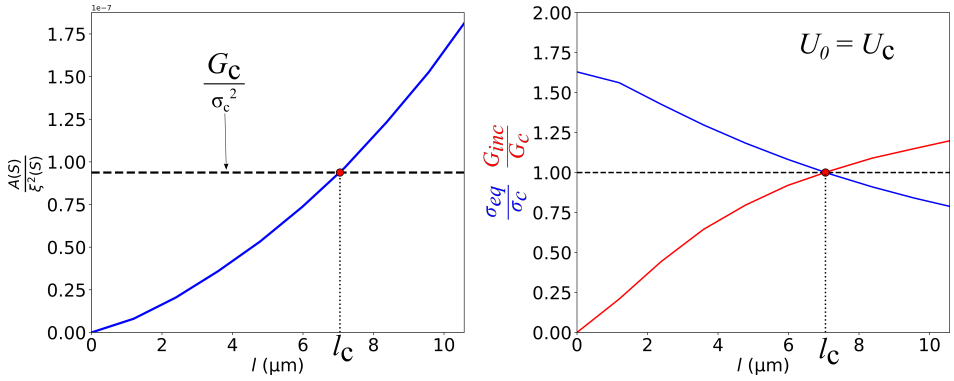

Figure 10: (Left) Graphical solution of Eqn. (7) allowing the determination of the initiation crack length l_c. (Right) Incremental energy release rate to fracture toughness and stress to strength ratios as a function of the crack surface for an imposed displacement equal to the initiation displacement (both criteria are fulfilled for $l = l_c$).

for α =1, G_c=15 J/m^2 and σ_c =400 MPa, both allowing the determination of the initiation length l_c.

5. Identification of interface strength and toughness

An example of the CC solution for micro- and macro-scale specimens has been presented in the previous section for given fracture parameters. This section is dedicated to the inverse identification of G_c, σ_c and τ_c by confrontation of the crack initiation forces predicted with the CC and measured experimentally.

5.1. Identification based on macro-scale experiments

We first investigate the parameter identification based only on macro-scale specimens. We define residuals that quantify the differences between the forces at crack initiation for SENB specimens predicted using the CC (denoted $F^{num}_{SENB}(G_c, \sigma_c, \alpha)$) and measured experimentally (denoted F^{exp}_{SENB}) :

$$R^2_{SENB} = \sum_{1}^{N_{SENB}} (F^{num}_{SENB}(G_c, \sigma_c, \alpha) - F^{exp}_{SENB})^2 \tag{9}$$

where N_{SENB} is the number of tested SENB specimens. We seek the parameter set that minimizes the residuals. As already mentioned in Section 3, the fracture toughness and strength can be varied during the post-processing of the FE calculations. Therefore it is

computationally inexpensive to compute the residuals for several parameter sets. Fig. 11(left) shows the residuals R_{SENB} as a function of G_c and σ_c for $\alpha = 1$. It can be observed that the residuals exhibits a minimum valley (highlighted by red stars in Fig. 11(left)) corresponding to several (G_c, σ_c) couples. The corresponding couples are also depicted for several values of α. For $\alpha > 1$, a similar curve as for $\alpha = 1$ is retrieved since in this case, the stress criterion reverts to a pure opening stress criterion and increasing α reverts to increasing τ_c, having no influence on the predicted force at crack initiation which is thus governed by the tensile strength. The insets in Fig. 11(right) show the incremental energy release rate to fracture toughness and stress to strength ratios as a function of the crack length for two different (G_c, σ_c) couples in the minimum valley. It can be observed that for the smallest value of G_c (corresponding to the largest value of σ_c), failure is driven by the stress criterion. Indeed, the stress criterion is only fulfilled on a short distance so that the crack initiation length is small, therefore in this case crack initiation is mainly driven by the stress criterion and thus by the material strength. Therefore, for a given α, it allows determining an upper bound for the tensile strength, equal to 470 MPa for $\alpha \geqslant 1$ for instance. For larger values of G_c and smaller values of σ_c, it can be observed in the inset that the initiation length is larger and crack initiation is driven by both the energy and the stress conditions. Fig. 12 shows the crack

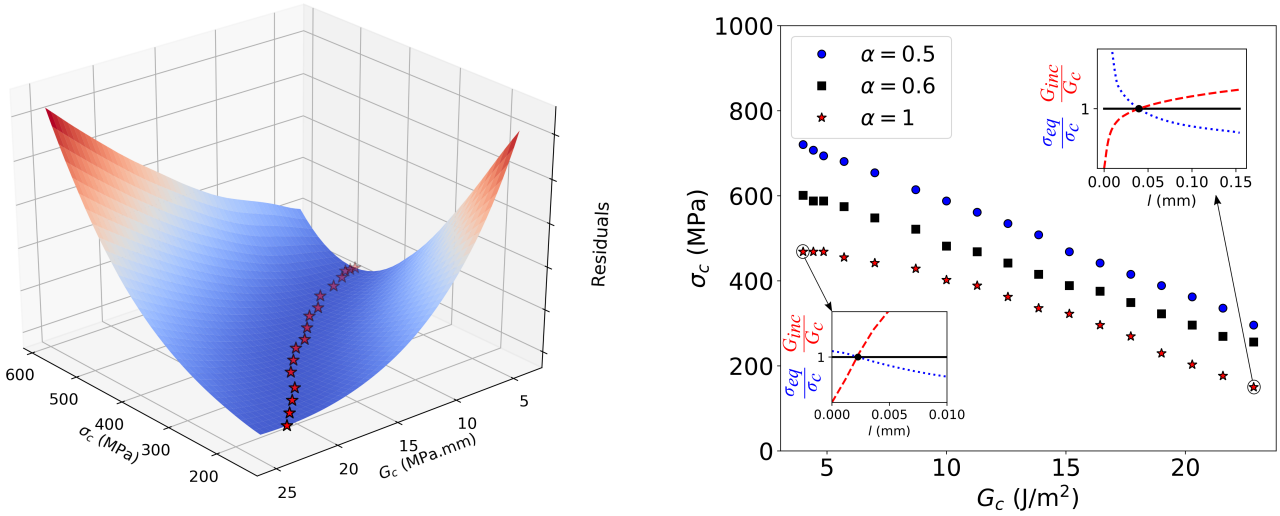

Figure 11: (Left) SENB Residuals as a function of strength and fracture toughness obtained for α=1 shear to tensile strength ratio, the minima are highlighted by red stars. (Right) (G_c, σ_c) couples minimizing the residuals for several α. The insets show the stress and energy criterion for two couples (G_c, σ_c).

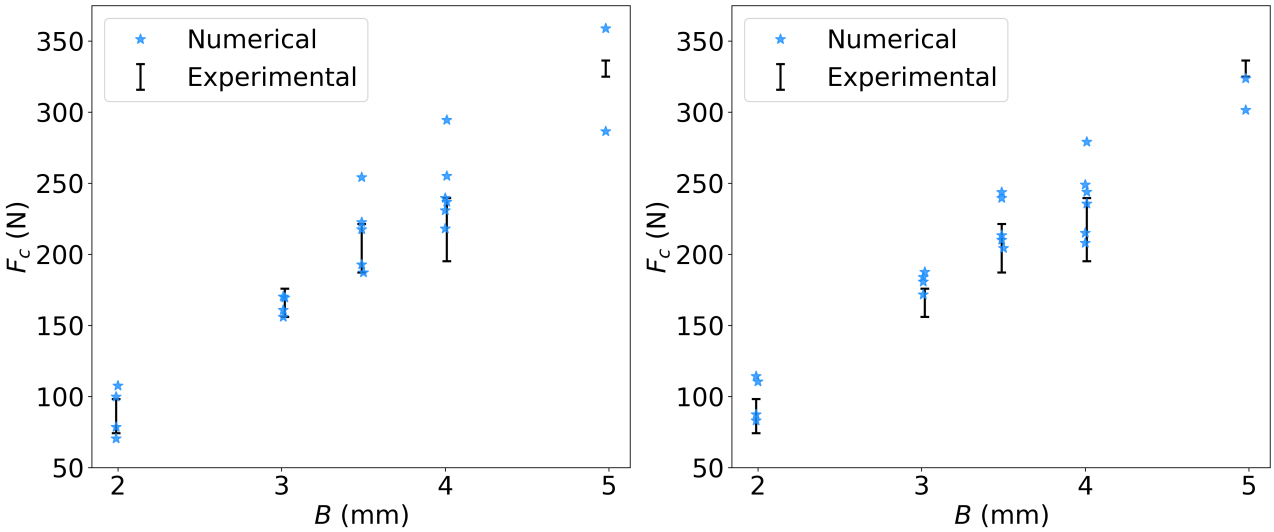

Figure 12: Forces at failure measured experimentally and predicted numerically using the coupled criterion for $\alpha = 1$ shear to tensile strength ratio and (Left) G_c=4 J/m^2, σ_c=468 MPa (Right) G_c=22 J/m^2, σ_c=163 MPa, corresponding to two couples minimizing the residuals (*cf.* insets in Fig. 11).

initiation forces as a function of the specimen thickness predicted for all the SENB specimens using the two (G_c, σ_c) couples corresponding to the insets in Fig. 11. An excellent agreement between the predicted and measured forces at initiation is obtained with both couples. The sole use of SENB test in the inverse identification approach thus does not allow determining a single optimal (G_c, σ_c, τ_c) set. Indeed, crack initiation force variation as a function of the specimen thickness in SENB specimens can be reproduced employing an infinity of couples (G_c, σ_c). It also defines an upper bound for the tensile strength for a given value of shear to tensile strength ratio, above which the predicted crack initiation forces deviate from that measured experimentally.

5.2. Identification based on micro-scale experiments

We investigate the parameter identification based only on micro-scale specimens. We define residuals that quantify the differences between the forces at crack initiation for micro-scale specimens predicted using the CC (denoted $F^{num}_{micro}(G_c, \sigma_c, \alpha)$) and measured experimentally (denoted F^{exp}_{micro}) :

$$R^2_{micro} = \sum_{1}^{N_{micro}} (F^{num}_{micro}(G_c, \sigma_c, \alpha) - F^{exp}_{micro})^2 \tag{10}$$

where N_{micro} is the number of tested micro-scale specimens. We seek for the parameter set that minimizes the residuals. Fig. 13 shows the residuals R_{micro} as a function of G_c and σ_c for $\alpha = 1$. It can be observed that the residuals also exhibits a minimum valley (highlighted by red stars in Fig. 13) corresponding to several (G_c, σ_c) couples. The corresponding couples are also depicted for other values of α. It can be observed that for the smallest values of σ_c, the minimum valley correspond to a constant value of G_c. The inset corresponding to σ_c = 40 MPa and G_c =6.2 J/m^2 reveals that, for small σ_c values, the stress criterion is fulfilled on almost all the area undergoing tension, therefore in this case crack initiation is mainly driven by the energy criterion and thus by the material fracture toughness. Therefore, it yields an upper bound for the fracture toughness, above which the failure force predicted with the CC strongly deviate from the one measured experimentally. For smaller values of σ_c corresponding to larger values of G_c, failure is driven by both the stress and the energy conditions (see the inset in Fig. 13).

Fig. 14 shows the crack initiation forces as a function of the interface angle θ predicted for all the micro-scale specimens using the two (G_c, σ_c) couples corresponding to the insets in Fig. 13. It can be noted that the difference between failure force corresponding to specimens with

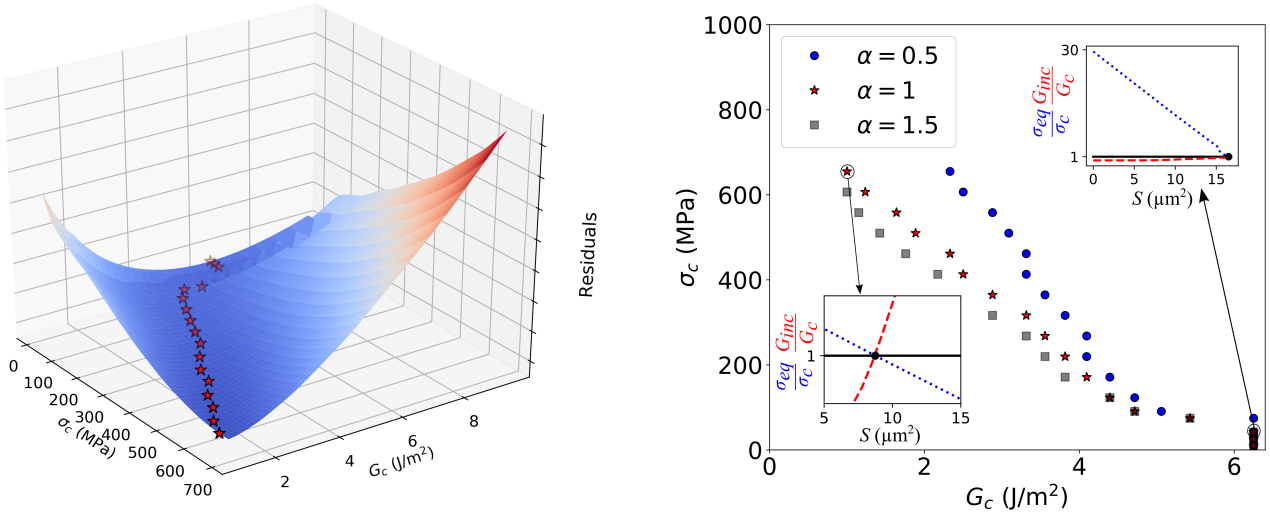

Figure 13: (Left) Micro-scale specimens residuals as a function of strength and fracture toughness obtained for α=1 shear to tensile strength ratio, the minima are highlighted by red stars. (Right) (G_c, σ_c) couples minimizing the residuals for several α. The insets show the stress and energy criteria for two couples (G_c, σ_c).

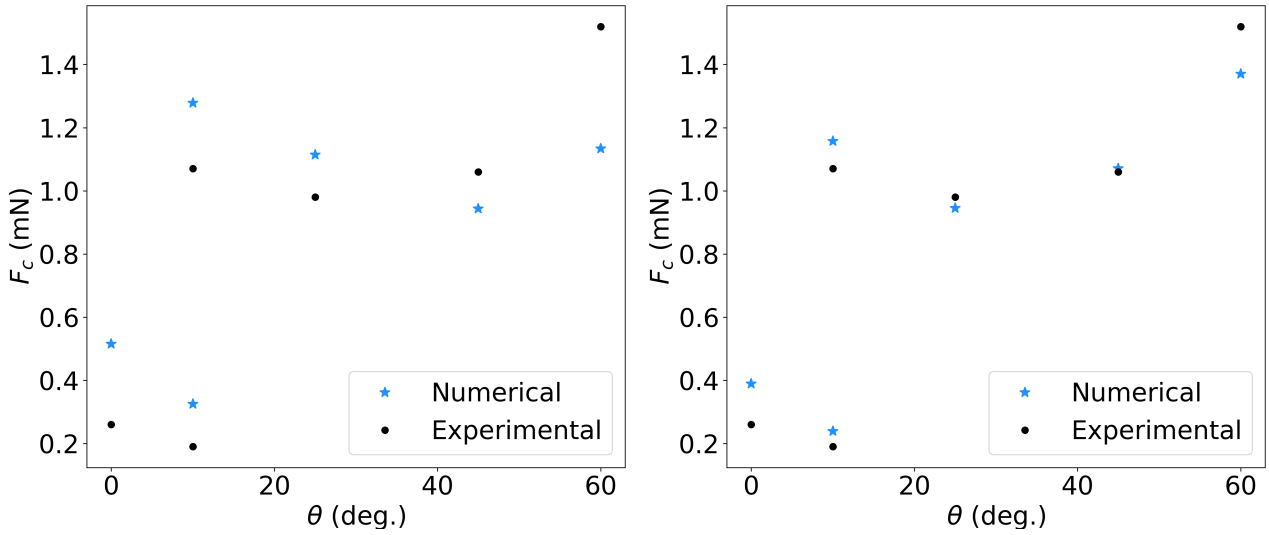

Figure 14: Forces at failure measured experimentally and predicted numerically using the coupled criterion for $\alpha = 1$ shear to tensile strength ratio and (Left) G_c=6.2 J/m^2, σ_c=40 MPa (Right) G_c=1 J/m^2, σ_c=655 MPa, corresponding to two couples minimizing the residuals (*cf.* insets in Fig. 13).

$\theta = 10$ deg. and $\theta = 12$ deg. results from the specimen dimensions that are significatively different (*cf.* Tab. 1).

5.3. Identification based on both macro- and micro-scale experiments

We now investigate the parameter identification based on both micro- and macro-scale specimens. Since the force levels in micro- and macro-scale specimens differ by several orders of magnitude, we define residuals that account for these differences by a weighted sum of the micro-scale and SENB residuals based on the force measurement uncertainty (*cf.* Sections 2.2 and 2.3) and the number of tested specimens:

$$R_T^2 = \frac{R_{SENB}^2}{\gamma_{SENB}^2 N_{SENB}} + \frac{R_{micro}^2}{\gamma_{micro}^2 N_{micro}} \tag{11}$$

We seek for the parameter set that minimizes the total residuals R_T. Fig. 15 shows the residuals R_T as a function of G_c and σ_c for $\alpha = 1$. It can be observed that the residuals exhibits a minimum (highlighted by red stars in Fig. 15) which allows determining the optimal (G_c, σ_c) couple for a fixed α. Fig. 15 also shows the variation of the residuals minimum as a function of the shear to tensile strength ratio α. The minimum of the residuals is reached for α =1.43, corresponding to the following optimal parameters:

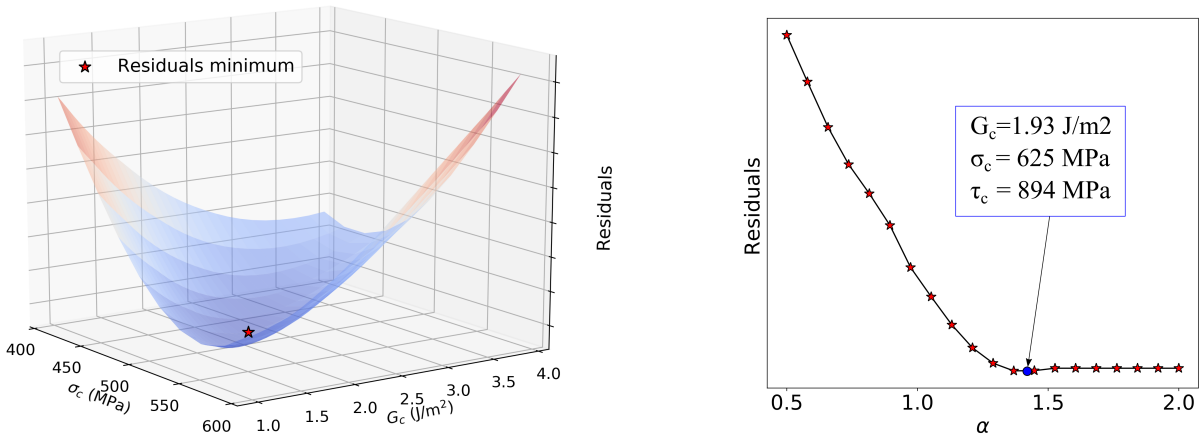

Figure 15: (Left) Residuals as a function of strength and fracture toughness obtained for α=1 shear to tensile strength ratio, the residuals minimum is highlighted by a red star. (Right) Residuals minimum as a function of α, the properties in the inset are given for the optimum reached for α=1.43.

. G_c=1.93 J/m^2

. σ_c=625 MPa

. τ_c=894 MPa

It can be noted that for $\alpha > 1.5$, the residuals reach a plateau which can be explained by the fact that for τ_c is sufficiently larger compared to σ_c so that the stress criterion only involves opening strength. The identified fracture toughness is slightly smaller than typical glass fracture toughnesses (4 to 30 J/m^2). Nevertheless, the identified fracture toughness seems reasonable since on the one hand, the interface may contain possible defects, and on the other hand, we could not determined whether failure occurs within the interface (cohesive failure) or at the interface between the platelet and the glass phase (adhesive failure). The forces at crack initiation for both SENB and micro-scale specimens predicted with the CC employing these parameters are shown in Fig. 16. It can be observed that the identified parameters allows reproducing the failure force for both micro-scale and SENB specimens. The proposed approach allows determining the interface fracture properties, indepently from the scale at which the material is studied. They can thus be used in numerical models for interface fracture in nacree-like alumina at both micro- and macro-scale.

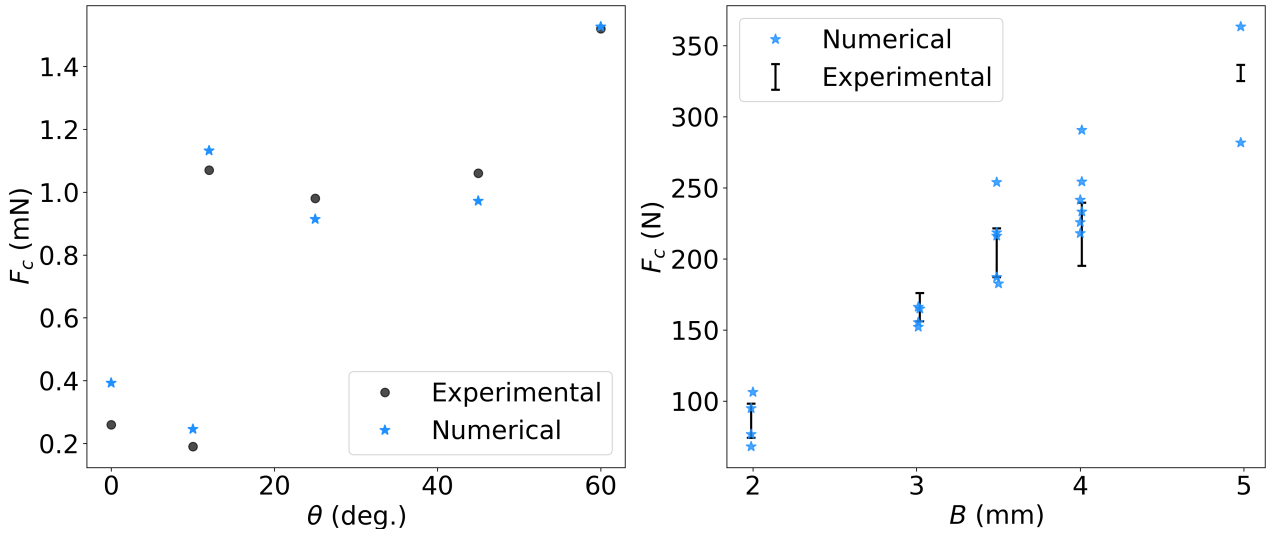

Figure 16: Force at failure measured experimentally and predicted numerically for (Left) micro-cantilever and (Right) SENB specimens using the coupled criterion with G_c=1.93 J/m^2, σ_c=625 MPa and τ_c=894 MPa.

6. Conclusion

We assess crack initiation in nacre-like alumina both at the micro- and macro-scale by means of micro-cantilever and SENB experiments. At both scales, the crack initiates at the interface between the platelets. Mixed mode crack initiation is studied at both scales since in micro-scale specimens, the interface is slanted with respect to the beam neutral axis and at the macro-scale, the interface between the platelets lies in the direction perpendicular to the specimen middle plane direction corresponding to pure opening. The coupled criterion allows modeling interface crack initiation at both scales, by means of 2D and 3D FE simulations. The sole use of SENB specimens yields an infinity of parameter sets for which the crack initiation forces predicted using the CC reproduce well the ones measured experimentally. Combining both micro-scale and SENB experiments in the inverse identification approach allows the determination of an optimal parameter set. The interface exhibits a 625 MPa tensile strength, 894 MPa shear strength and a 1.93 J/m^2 fracture toughness. Employing these parameters, the crack initiation forces predicted by the coupled criterion are in good agreement with the one measured experimentally at both scales. The quantitative determination of the interface fracture properties should help the design and optimization of this class of brick-and-mortar materials.

Acknowledgements

References

[1] J. Currey, J. Taylor, The mechanical behaviour of some molluscan hard tissues, J. Zool. (London) 173 (1974) 395–406.

[2] F. Barthelat, H. Espinosa, An experimental investigation of deformation and fracture of nacre-mother of pearl, Exp. Mech. 47 (2007) 311–324.

[3] R. Wang, Z. Suo, A. Evans, N. Yao, I. Aksay, Deformation mechanisms in nacre, J. Mater. Res. 16 (9) (2001) 2485–2493.

[4] R. Rabei, S. Bekah, F. Berthelat, Failure mode transition in nacre and bone-like materials., Acta Biomater. 6 (2010) 4081–4089.

[5] F. Barthelat, H. Tang, P. Zavattieri, C. Li, H. Espinosa, On the mechanics of mother-of-pearl: A key feature in the material hierarchical structure, J. Mech. Phys. Solids. 55 (2007) 306–337.

[6] F. Bouville, Strong and tough nacre-like aluminas: Process-structure-performance relationships and position within the nacre-inspired composite landscape, J. Mater. Research (2019) 1–19doi:10.1557/jmr.2019.418.

[7] F. Bouville, E. Maire, S. Meille, B. Van de Moortèle, A. Stevenson, D. S., Strong, tough and stiff bioinspired ceramics from brittle constituents, Nat Mater 13 (2014) 508–514.

[8] E. Feilden, C. Ferraro, Q. Zhang, E. García-Tunon, E. D'Elia, F. Giuliani, 3d printing bioinspired ceramic composites, Sci Rep 7 (2017) 13759.

[9] O. Picot, V. Rocha, C. Ferraro, N. Ni, E. D'Elia, S. Meille, J. Chevalier, T. Saunders, T. Peijs1, M. Reece, E. Saiz, Using graphene networks to build bioinspired self-monitoring ceramics, Nature comm 8 (2017) 14425.

[10] M. Begley, N. Philips, B. Compton, D. Wilbrink, R. Ritchie, M. Utz, Micromechanical models to guide the development of synthetic brick and mortar composites, J. Mech. Phys. Solids 60 (2012) 1545–1560.

[11] L. Dimas, M. Buehler, Tough and stiff composites with simple building blocks, J. Mater. Res. 28 (2013) 1295–1303.

[12] F. Barthelat, Designing nacre-like materials for simultaneous stiffness, strength, and toughness: Optimum materials, composition, microstructure and size., J. Mech. Phys. Solids 73, (2014) 22–37.

[13] N. Abid, M. Mirkhalaf, F. Barthelat, Discrete-element modeling of nacre-like materials: Effects of random microstructures on strain localization and mechanical performance, J. Mech. Phys. Solids 112 (2018) 385–402.

[14] K. Radi, D. Jauffres, S. Deville, C. Martin, Strength and toughness trade-off optimization of nacre-like ceramic composites, Compos. Part B 183 (2020) 107699.

[15] H. Le Ferrand, F. Bouville, T. Niebel, A. Studart, Magnetically assisted slip casting of bioinspired heterogeneous composites, Nature mat. (2020) 1172–1781doi:10.1038/NMAT4419.

[16] H. Saad, K. Radi, T. Douillard, D. Jauffres, C. Martin, S. Meille, S. Deville, A simple approach to bulk bioinspired tough ceramics, https://hal.archives-ouvertes.fr/hal-02493649 (2020).

[17] E. Feilden, T. Giovannini, N. Ni, C. Ferraro, E. Saiz, L. Vandeperre, Micromechanical strength of al_2o_3 platelets, Scripta Mater 131 (2017) 55–58.

[18] A. Doitrand, R. Henry, J. Chevalier, S. Meille, Revisiting the strength of micron-scale ceramic platelets, J. Am. Cer. Soc. (2020). doi:10.1111/jace.17148.

[19] D. Leguillon, Strength or toughness? a criterion for crack onset at a notch, Eur. J. Mech. - A/Solids 21(1) (2002) 61–72.

[20] A. Doitrand, E. Martin, D. Leguillon, Numerical implementation of the coupled criterion: Matched asymptotic and full finite element approaches, Fin. Elem. Anal. Des. 168 (2020) 103344.

[21] R. Henry, H. Saad, A. Doitrand, S. Deville, S. Meille, Interface failure in nacre-like alumina, Submitt. J. Eur. Cer. Soc. https://doi.org/10.26434/chemrxiv.12006270.v1 (2020).

[22] E. Martin, D. Leguillon, N. Carrère, A twofold strength and toughness criterion for the onset of free-edge shear delamination in angle ply laminates, Int. J. Sol. Struct. 47 (2010) 1297–1305.

[23] E. Martin, D. Leguillon, N. Carrère, A coupled strength and toughness criterion for the prediction of the open hole tensile strength of a composite plate, Int. J. Sol. Struct. 49(26) (2012) 3915–3922.

[24] A. Doitrand, C. Fagiano, N. Carrère, V. Chiaruttini, M. Hirsekorn, Damage onset modeling in woven composites based on a coupled stress and energy criterion, Engng. Fract. Mech. 169 (2017) 189–200.

[25] A. Doitrand, C. Fagiano, F. Hild, V. Chiaruttini, A. Mavel, M. Hirsekorn, Mesoscale analysis of damage growth in woven composites, Compos. Part A 96 (2017) 77–88.

[26] V. Mantič, Interface crack onset at a circular cylindrical inclusion under a remote transverse tension. application of a coupled stress and energy criterion, Int. J. Sol. Struct. 46 (2009) 1287–1304.

[27] V. Mantič, I. García, Crack onset and growth at the fibre-matrix interface under a remote biaxial transverse load. application of a coupled stress and energy criterion, Int. J. Sol. Struct. 49 (2012) 2273–2290.

[28] N. Carrère, E. Martin, D. Leguillon, Comparison between models based on a coupled criterion for the prediction of the failure of adhesively bonded joints, Eng. Fract. Mech. 138 (2015) 185–201.

[29] N. Stein, P. Weigraeber, W. Becker, A model for brittle failure in adhesive lap joints of arbitrary joint configuration, Compos. Struct. 133 (2015) 707–718.

[30] J. Felger, P. Rosendahl, D. Leguillon, W. Becker, Predicting crack patterns at bi-material junctions: A coupled stress and energy approach, Int. J. Sol. Struct. 164 (2019) 191–201.

[31] A. Doitrand, D. Leguillon, Comparison between 2D and 3D applications of the coupled criterion to crack initiation prediction in scarf adhesive joints, Int. J. Adh. Adh. 85 (2018) 69–76.

[32] A. Doitrand, D. Leguillon, 3D application of the coupled criterion to crack initiation prediction in epoxy/aluminum specimens under four point bending, Int. J. Sol. Struct 143 (2018) 175–182.

[33] M. Muñoz Reja, L. Távara, V. Mantič, P. Cornetti, A numerical implementation of the coupled criterion of finite fracture mechanics for elastic interfaces, Theor. App. Fract. Mech. (2020). doi:10.1016/j.tafmec.2020.102607.

[34] R. V. G. Sundara Rao, Elastic constants of alumina, Proc. Indian Acad. Sci. A 29 (1949) 352–360.

[35] A. Doitrand, D. Leguillon, Numerical modeling of the nucleation of facets ahead of a primary crack under modeI+III, Int. J. Fract. 123(1) (2018) 37–50.

[36] A. Doitrand, R. Estevez, D. Leguillon, Experimental characterization and numerical modeling of crack initiation in rhombus hole pmma specimens under compression, Eur. J. Mech. Sol. 76 (2019) 290–299.